# Evolution of the Pore-Pressure Field around a Moving Conical Penetrometer of Finite Size

Michael Fitzgerald[1] and Derek Elsworth[2]

**Abstract:** A solution is developed for the evolution of buildup, steady, and postarrest dissipative pore-fluid pressure fields that develop around a finite-radius conical penetrometer advanced in a saturated linearly elastic porous medium. The analog with cone penetrometer testing is direct and is used to enable continuous distributions of permeability and diffusivity to be determined with depth. This analysis reveals the direct dependence of penetration rate on the induced fluid pressure field magnitudes, and predicts that a penetration rate threshold limit exists with respect to pore-pressure generation. This represents the essence of a partially drained system. The developed pore-pressure field is determined to be a function of the dissipation rate of the material, the penetration rate, and the storage effects of the advecting medium. Analysis of the pore-pressure field under start-up conditions reveals that the time required to reach steady state is strongly influenced by the penetration rate and the pressure-dissipation properties of the material. Analysis of the developed stable pressure fields illustrates the inversely proportional relationship that exists between penetration rate and pore-pressure magnitudes at the cone surface; representing the influence of storage in the medium on stable pore-pressure magnitudes. Stable pressure fields below the penetration threshold limit, $U_D \leqslant 10^{-1}$, form a spherical response around the cone tip transitioning to an elongated radial response for penetration rates above this limit. Postarrest analysis indicates that the prearrest penetration rate strongly influences the dissipation rate and pattern of dissipation. The developed analysis can be correlated with CPTu-recovered data to independently evaluate permeability magnitudes during steady penetration.

## Introduction

The cone penetration test (CPTu) is a widely used tool for characterizing mechanical and transport properties of soils in situ (Lunne et al. 1997), through depth-continuous profiles of end-bearing stress, sleeve-frictional stress, and absolute pore-fluid pressure. Pore-pressure magnitudes are typically measured at the cone tip (U1), the cone shoulder (U2), or along the shaft (U3 or U4), and these measurements are known to differ due to the physical geometry of the penetrometer and the material properties of the advecting soil.

Empirical correlations have been developed for qualitatively defining soil types (Robertson et al. 1986) along with analytical methods to understand the mechanics of the processes involved with the penetrometer insertion. Primarily these involve the strain and pressure fields that develop around the cone during advance-ment. These analytical methods can be broadly classified into two groups, static and migrating models. Static models mainly relate to cavity expansion results for spherical (Ladanyi 1963) and cylindrical (Randolph and Wroth 1979) geometries, and are capable of incorporating frictional behavior (Vesic 1972) and shear induced pore pressures (Chen and Mayne 1994). They have been applied to define the initial undrained distributions of pore pressure and their subsequent dissipation (Chen and Mayne 1994; Randolph and Wroth 1979; Torstensson 1977), and have been used in determining the hydraulic diffusivity of soils. Though a limitation exists for cavity expansion models to reproduce pore-pressure fields that result at the cone tip, the more pressing limitation is the inability to accommodate the precise tip geometry of the penetrometer. Pore-pressure fields that develop around a steady penetrating cone have been shown to be strongly dependent on the shape of the cone tip and the degree of taper (Levadoux and Baligh 1986). Thus, the locations of the pressure sensing element inlets are important (Robertson et al. 1992). These limitations on using cavity expansion methods to represent these facets make their use in data reduction problematic.

Migrating models accommodate the noninertial dynamic effects of the moving penetrometer tip. Important criteria are (1) accurately determining the evolving tip-local strain field and (2) accommodating the partial drainage condition by allowing simultaneous pore-pressure generation and dissipation. Tip-local strain fields may be determined from considerations of kinematic failure mechanisms (Baligh and Scott 1976; Drescher and Kang 1987) and by considering steady plastic flow (Acar and Tumay 1986; Tumay et al. 1985), with appropriate pore-pressure parameters used to determine the instantaneous pore-pressure distributions

[1]Post-Doctoral Researcher, Dept. of Energy and Mineral Engineering, Center for Geomechanics, Geofluids, and Geohazards, Penn State Univ., University Park, PA 16802 (corresponding author). E-mail: mxf218@psu.edu

[2]Professor, Dept. of Energy and Mineral Engineering, Center for Geomechanics, Geofluids, and Geohazards, Penn State Univ., University Park, PA 16802. E-mail: elsworth@psu.edu

(Biot and Willis 1957; Skempton 1954). A strain-path analysis (Baligh 1985) was developed to circumvent many of the complexities involved in defining the large strain field by neglecting the rigorous solution of equilibrium equations, but yielding a strain distribution field based on the applied displacement (or displacement-rate) boundary conditions. This is shown to provide sufficient predictions of undrained pore-pressure generation (Baligh and Levadoux 1986; Levadoux and Baligh 1986), adequately incorporating cone geometry effects, and may be applied equally to complex and relatively straightforward (Teh and Houlsby 1991) material models.

Dislocation-based methods (Elsworth 1991, 1992, 1998) are alternative to strain-path methods and enable both the undrained and partially drained behaviors to be accommodated, though a pseudoelastic material behavior is used which negates the development of a true tip-local process zone. Also the analyses are for moving point dislocations within the poroelastic medium, and do not adequately represent the influence of the tip geometry and its finite size on pressure generation. Despite these limitations, the penetration induced fluid pressure response evaluated from the dislocation analysis closely matches the undrained behavior observed (Baligh and Levadoux 1986) and replicated by other methods (Levadoux and Baligh 1986; Teh and Houlsby 1991) and are not restricted to undrained behavior alone.

This study advances the current body of knowledge regarding the development of pore-pressure fields resulting from penetrometer advance in a saturated poroelastic medium by accurately accommodating the important effects of cone tip geometry and partial drainage of the pore-pressure response. The influence of partial drainage is examined here for start-up, steady-state, and postarrest dissipation conditions illustrating the behavioral dependence of the pore-pressure field on the drainage state of the penetrating cone tip. This study establishes a dimensionless analysis through which the competition between pore-pressure generation (via strain rate) and dissipation (via diffusivity) may be examined and used to understand the development of pore-pressure responses at the penetrometer tip. This analysis supplements previous steady-state characterizations (Elsworth and Lee 2005) which have been proven useful in recovering profiles of permeability data from peak pore-pressure magnitudes measured concurrent with advance.

## Analysis

The pore-fluid pressure fields that develop around a conical tipped penetrometer advanced within a saturated porous soil are examined. The process is best viewed in a Lagrangian frame of reference, where the origin is fixed at the penetrometer tip and the saturated medium advects past the static penetrometer. This reference frame is selected throughout. The steady flow field within the soil is evaluated from Stokes flow around the penetrometer. The pore-pressure buildup and dissipation is followed by considering fluid transport within the migrating porous medium, where pressure generation is approximated by the volume displaced by the inserted penetrometer and applied at the tip face (Elsworth 1998). This analysis is described in the following and implemented as a finite-element analysis. The system is then examined to provide a detailed description of the mechanisms of fluid pressure generation and dissipation, and the appropriate parametric controls on this behavior.

### Pore-Pressure Response in Moving Coordinates

Conservation of the flowing mass is defined in terms of the mass of the flowing soil-water mixture, $\rho$, and its velocity of transport of the fluid, $v_i^f$, with respect to the coordinate system, $x_i$, and time, $t$, as

$$\frac{D\rho}{Dt} + \rho \frac{\partial v_i^f}{\partial x_i} = 0 \qquad (1)$$

where the material derivative is defined as $D\rho/Dt=(\partial \rho/\partial t)+[v_i(\partial \rho/\partial x_i)]$, in terms of the velocity of the fluid-solid mixture, $v_i$, then in a Lagrangian frame of reference, migrating with the bulk motion of the mixture, substituting into Eq. (1) yields

$$\frac{\partial \rho}{\partial t} + v_i \frac{\partial \rho}{\partial x_i} + \rho \frac{\partial v_i^f}{\partial x_i} = 0 \qquad (2)$$

This statement may be recast in terms of fluid pressures by defining appropriate constitutive relations linking fluid pressures with flow velocities and changes in mass due to the release of fluid from storage. The first defines the rate of transport of the fluid relative to the soil mass through Darcy's law as

$$v_i^f = -\frac{k_i}{\mu} \frac{\partial p}{\partial x_i} \qquad (3)$$

where flow is driven by the fluid pressure, $p$, and moderated by the directional permeability of the soil, $k_i$, and the dynamic viscosity of the fluid, $\mu$. The second defines the change in mass of the fluid-solid system due to the drained expulsion of fluid with changes in fluid pressure. The volume compressibility of the mixture, $m_v$, is defined as

$$m_v = \frac{1}{\rho} \frac{\partial \rho}{\partial p} \qquad (4)$$

and represents the change in volume resulting from a unit increase in fluid pressure or equivalent decrease in mean effective stress. Therefore, volume compressibility is related to drained bulk modulus, $K$, and the product of porosity and fluid compressibility, $\phi\beta_f$, by the relation $m_v=\phi\beta_f+1/K$. It is noteworthy that the volume compressibility, $m_v$, is not the one-dimensional constrained compressibility, as it is often defined, but is the unconstrained response to a change in mean stress, including the minor influence of the compressibility of the fluid. This compressibility enables changes in mass balance to be defined within the system, both in time, as

$$\frac{\partial \rho}{\partial t} = \rho m_v \frac{\partial p}{\partial t} \qquad (5)$$

and in space, as

$$\frac{\partial \rho}{\partial x_i} = \rho m_v \frac{\partial p}{\partial x_i} \qquad (6)$$

Substituting Eqs. (3), (5), and (6) into Eq. (2) yields the final relation

$$m_v \frac{\partial p}{\partial t} + m_v v_i \frac{\partial p}{\partial x_i} - \frac{\partial}{\partial x_i} \frac{k_i}{\mu} \frac{\partial p}{\partial x_i} = 0 \qquad (7)$$

which together with the convective flux, $q_i$, and pressure boundary conditions

$$q_i = -\frac{k_i}{\mu}\frac{\partial p}{\partial x_i} + m_v p v_i, \quad p = p_{\text{defined}} \qquad (8)$$

gives a full system of equations for solution.

## Dimensionless Form

For convenience, the governing relation of Eq. (7) and the associated boundary conditions of Eq. (8) may be represented in terms of the dimensionless variables. In this we select pressure relative to the reference far-field pressure, $p_s$, and a characteristic length given in this case by the radius of the probe, $a$. Furthermore, the mass compressibility may be related to permeability via the hydraulic diffusivity as $c = (k_i/\mu)(1/m_v) = (k_i/\mu)K$. Substituting these quantities into Eq. (7) defines the governing expression as

$$\frac{\partial P_D}{\partial t_D} + U_D\left(\frac{v_i}{U}\right)\frac{\partial P_D}{\partial x_D} - \frac{\partial}{\partial x_D}\frac{\partial P_D}{\partial x_D} = 0 \qquad (9)$$

In terms of dimensionless pressure, $P_D$

$$P_D = \frac{k_i}{\mu}\frac{(p - p_s)}{Ua} \qquad (10)$$

dimensionless penetration rate, $U_D$

$$U_D = \frac{Ua}{C_v} \qquad (11)$$

dimensionless time, $t_D$

$$t_D = \frac{C_v t}{a^2} \qquad (12)$$

and dimensionless coordinate system, $x_D$

$$x_D = x_i/a \qquad (13)$$

Similarly, the boundary conditions may be cast in dimensionless form, as

$$Q_D = -\frac{\partial P_D}{\partial x_D} + U_D\left(\frac{v_i}{U}\right)P_D, \quad P_D = P_{D\,\text{defined}} \qquad (14)$$

where $Q_D = q_i/U$.

## Flow Field around the Cone Tip

Separate from the pressure diffusion equation, the flow field of the mixture must be defined. The momentum balance and continuity equations are

$$\rho\frac{\partial v_i}{\partial t} + \rho v_i\frac{\partial v_i}{\partial x_i} = \rho g\frac{\partial x_i}{\partial x} - \frac{\partial P}{\partial x_i} + \mu\frac{\partial}{\partial x_i}\frac{\partial v_i}{\partial x_i} \qquad (15)$$

and

$$\frac{\partial v_i}{\partial x_i} = 0 \qquad (16)$$

and are applied with the appropriate boundary conditions. Importantly, the fluid pressures driving the flow are not the same as in the pressure diffusion equation, and are merely used to condition flow at the desired velocity past the probe, in the far field. For typical anticipated velocities, the convective accelerations and body forces are typically small in comparison to viscous effects, and the system may be adequately represented by steady Stokes flow with $\nabla P = \mu\nabla^2\mathbf{v}$ and $\nabla\cdot\mathbf{v} = 0$.

## Boundary Conditions

For an axisymmetric flow system, with the medium moving at velocity, $U$, boundary conditions may be defined for the CPTu geometry, where the fluid is injected through the curved surface of a cylinder of radius, $a$, and length, $l$, at velocity, $q$. The appropriate dimensionless flux $Q_D = q/U$ may be defined as

$$\text{CPTu:} \quad Q_D^{\text{CPTu-Blunt}} = \frac{a}{2l} = \frac{1}{2l_D} \qquad (17)$$

where the tip is tapered at semi-interapical angle $\theta$ and the taper exists over length $l$, then the injected fluid may be applied over the face of this tapered cone. For a coordinate system $\chi, r$ centered on the tip, with $\chi$ positive in the direction of increasing tip taper, the volume of the tapered tip displaced per unit length of travel is (Elsworth 1998)

$$V = 2\pi\tan^2\theta U\chi d\chi \qquad (18)$$

where this volume is applied over the area of the cone surface, the velocity flux is given by $q = V/2\pi a$ where $a$=radius to the tapered face of the probe, where surface length $dS$ is related to $d\chi$ as $d\chi = \tan\theta dS$, to yield

$$q = U\sin\theta dS \qquad (19)$$

or $U\sin\theta$ per unit length. This may be nondimensionalized to give

$$Q_D^{\text{CPTu-tapered}} = \frac{q}{U} = \sin\theta \qquad (20)$$

when applied normal to the tapered surface over the length of the tip $l_D = 1/\tan\theta$.

## Finite-Element Approach

The equations for Stokes flow and for Darcy transport within an advecting porous medium are solved in standard finite-element format (Comsol Multiphysics, Version 3.3) for a two-dimensional axisymmetric mesh centered about the cone. Fig. 1 illustrates the model geometry and the mesh density with a refined mesh density near the probe surface with a minimum element size of $\sim 30\times 10^{-6}$ of the probe radius. The mesh on the interior boundary is an order of magnitude denser than the far field (a total of 1,702 elements contrasting the 113 elements on the far-field boundary). The mesh comprises 25,303 triangular quadratic elements comprising 170,826 degrees of freedom. Mesh deformation due to penetration of the probe, a potential problem, is mitigated by not moving the mesh but rather prescribing the soil flow field as migrating through the mesh; thus the elements do not deform. This migration of the soil flow field is controlled through Stokes flow where the soil influx and efflux boundaries are defined as pressure boundaries, and the resulting flow velocities indexed to the required average far-field velocity by adjusting the ratio of the pressure drop to the assigned viscosity of the flowing medium. Also the tip and shaft boundaries together with the parallel far-field boundary are defined by slip conditions. For the Darcy flow problem, the vertical boundaries are prescribed as zero flux boundaries. The inflow boundary is prescribed as zero induced excess pressure, and the efflux boundary is a convective flux condition. The local flow velocities recovered from the Stokes solution are applied spatially to the Darcy flow geometry.
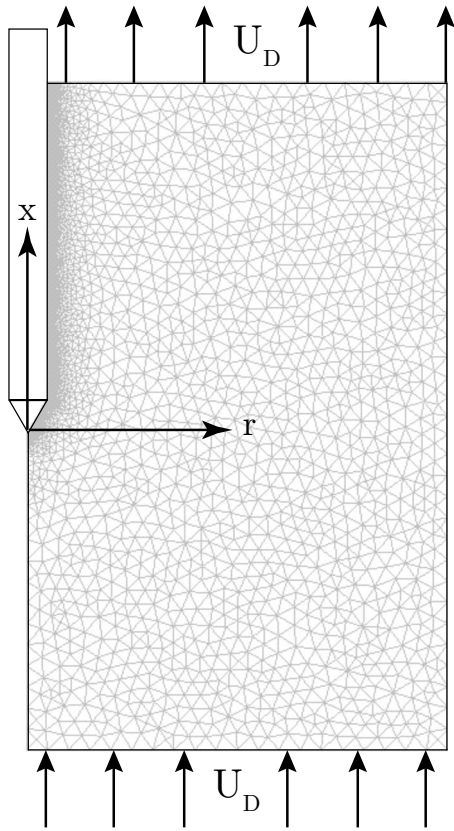
**Fig. 1.** Finite-element mesh local to the penetrometer representing mesh size distribution across the geometry. Minimum element size is $30 \times 10^{-6}$ of the vertical height of the geometry. The radius of the penetrometer is 1 and the cone interapical angle is 60°. Note that material advects past the static cone in the positive $x$ direction at nondimensional penetration rate, $U_D$.

### *FEM Verification*

Although no comparable analytical solutions exist for the geometry of a tapered penetrometer of finite size, moving within saturated porous medium, solutions are available for a moving point dislocation (Elsworth 1991, 1992). This is broadly representative of the pore-pressure field anticipated around a blunt penetrometer, and may be compared with the numerical solution. The steady-state induced pore-pressure field is given as

$$P_D R_D = \frac{1}{4} e^{-U_D(R_D - x_D)/2} \qquad (21)$$

with $R_D = R/a$, where $a =$ radius of the cone and $R^2 = x^2 + r^2$ (Elsworth 1991). Fig. 2 illustrates the locations of the different positions in reference to the cone tip and shaft. With the origin superimposed at the U2 position on the shoulder of the cone shaft $r = a = 1$ and $x = 0$. Hence, along the horizontal radial trace, $x_D = 0$, the variation in dimensionless pore pressure is given as $P_D = (1/4R_D)e^{-(U_D R_D)/2}$. A comparison of analytical and numerical results is shown in Fig. 3 for dimensionless penetration rates $U_D = 10^{-1}$ and $U_D = 10^{0}$. Overall, a review of the figure shows that the general trend of pressure decay with radial increase from the source location is upheld and a close match with the previously documented relationship is observed. The slight deviations that exist between the numerical and analytical results are likely the result of the strong influence of the cone tip on the induced pressure field. The dislocation analysis (Elsworth 1991, 1998) did not
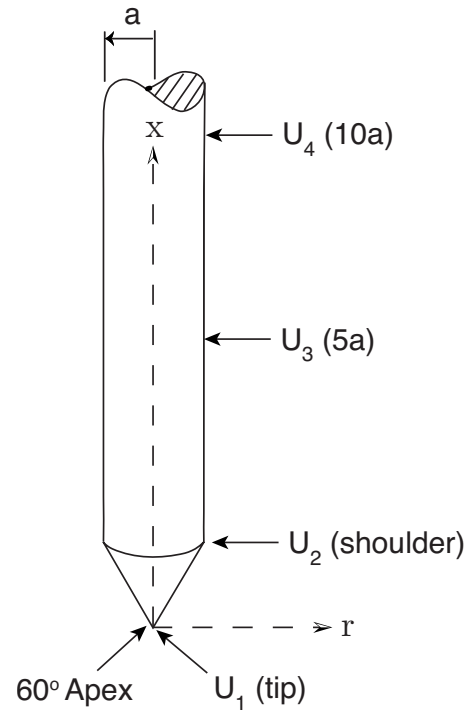


**Fig. 2.** Geometry of conical cone tip showing location of pore-pressure measurement ports (U1, U2, U3, and U4) and the orientation of the coordinate system

adequately represent this influence. In addition, to provide further verification of the model results, the FEM simulations are compared with CPTu data obtained from centrifuge tests as well as field data presented in later sections.

## Parametric Analysis

The pressure fields predicted by this model for a moving tapered penetrometer of finite size are reported in the following. The
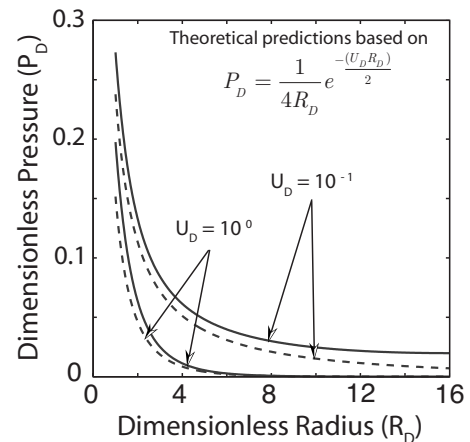


**Fig. 3.** Decay of dimensionless pressure radially away from the U2 location for the finite-element results compared with previously documented theoretical results (Elsworth 1991). The solid lines are used to represent the radial pressure decay as predicted by the model and the dashed lines are for the theoretical prediction pressure decay relationship determined by Elsworth (1991).

analyses consider pressure buildup, the resulting steady pressure field, and pressure dissipation following arrest for dimensionless penetration rates in the range $10^{-2} \leq U_D \leq 10^3$. Importantly, this range is selected as it bounds the transition from static to moving response ($U_D \sim 10^0$) where the pore-pressure field transitions from spherically symmetric ($U_D < 10^0$) to radially symmetric ($U_D > 10^0$). Profiles of induced pressures are shown around the penetrometer, and codified for buildup, steady-response, and postarrest dissipation relative to the U1, U2, and shaft mounted locations U3 and U4 ($x_D = 5$ and $x_D = 10$, respectively) as noted in Fig. 2.

### Soil Drainage States

The following analyses of the start-up, steady-response, and postarrest pore-pressure responses for a penetrating probe in a poroelastic medium rely heavily on the concept of dimensionless penetration rate, $U_D$, defined in Eq. (11) as the product of the penetration rate of the probe with the probe radius normalized by soil diffusivity. $U_D$ is a critical component of the following analyses as it serves an index to describe the drainage condition of the soil resulting from the competing processes of pore-pressure generation due to penetration rate and probe size, with pore-pressure dissipation due to the soils fluid transport properties (diffusivity). The penetration response is considered fully drained ($U_D \leq 10^{-2}$) when the generation of pore pressure is significantly less than the rate at which the induced pore pressures can dissipate. Under these conditions the pore-pressure field is governed by the rate of dissipation and is essentially independent of the penetration rate. The alternate scenario is fully undrained ($U_D \leq 10^2$) where the rate of pore-pressure generation is significantly greater than the rate of pore-pressure dissipation. Here the induced pore-pressure field is governed by the undrained shear strength of the soil as induced pore pressures exceed the soil shear strength causing localized failure limiting the peak pore-pressure magnitude. This relationship has been observed through miniature-CPTu experiments conducted with in the confines of a centrifuge strongbox (Randolph and Hope 2004).

### Start-Up Response

The evolving pore-pressure responses due to penetration start-up are shown in Fig. 4 [(a.1)–(c.1)] for dimensionless pore pressure ($P_D$) and for dimensional pore pressure ($P_D U_D = m_v \Delta P$) in Fig. 4 [(a.2)–(c.2)] with respect to the product of dimensionless time and penetration rate [$t_D U_D = (U/a)t$] for the U1, U2, and U3 recording locations, respectively.

Advancement of the penetrometer in a saturated porous medium results in the compression of the soil matrix directly ahead of the advancing cone tip and causes the pore-fluid pressures to build within the soil matrix surrounding the cone tip. Fig. 4 [(a.1)–(c.1)] shows the generation of pore pressure through a series of curves with each representing the systematic change in soil drainage conditions and illustrate how the pore-pressure fields develop with time. Fig. 4 [(a.2)–(c.2)] shows these trends recast in dimensional pressures.

In general, the observed relations from these pore-pressure generation traces show that as soil drainage conditions are decreased, marked by order of magnitude increases in $U_D$, the peak magnitude of steady-state pressure for each $U_D$ trace increases for all measuring positions along the cone surface. These traces show an evolving pore-pressure field that initiates at low excess fluid pressure and subsequently develops to stable magnitudes with
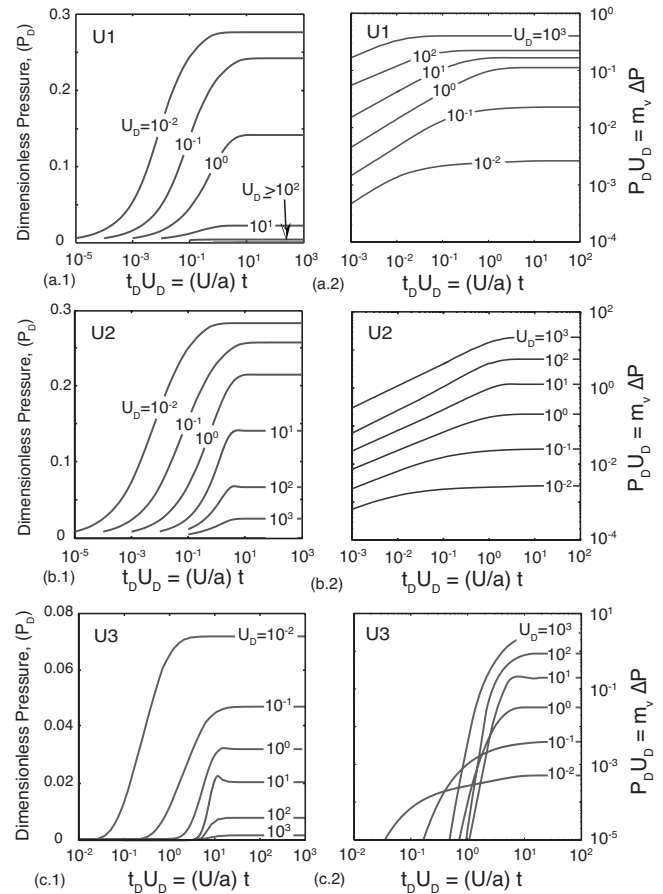


**Fig. 4.** Dimensionless pressure ($P_D$) magnitudes induced at the (a) U1; (b) U2; and (c) U3 locations along the penetrometer surface from the initiation of advance (start-up) shown relative to dimensionless time normalized by penetration rate ($t_D U_D$)

increasing time. The calculated magnitudes of the pore-pressure fields, for all measurement locations, rise to a peak steady threshold when $U_D \leq 10^{-2}$. This lower threshold marks the boundary where the induced pore-pressure fields transition from a dissipation governed response to a strain-rate governed response. Below $U_D \leq 10^{-2}$ the system is essentially drained and the pore-pressure magnitudes measured at all points on the cone surface are very low as the generation of pore pressure is limited due to the highly diffusive system when compared to the strain rate. Above this fully drained limit, $U_D > 10^{-2}$, a systematic increase in the stable peak pore-pressure magnitudes for each order-of-magnitude increase in $U_D$ is observed. This increase in peak $P_D U_D$ magnitudes results from the drainage condition of the soil surrounding the penetrating probe changing from fully drained ($U_D \leq 10^{-2}$) to undrained ($U_D \geq 10^2$) transiting through the partially drained regime as the diffusivity of soil decreases.

### Steady-State Response

Peak steady-state dimensionless pore pressures induced at the U1, U2, U3, and U4 positions for varied penetration rates in the range $10^{-2} \leq U_D \leq 10^3$ are shown in Fig. 5(a). Fig. 5(b) shows the dimensionless pressures traces recast in dimensional form and compared against centrifuge data obtained from a sample of 75% kaolin mixed with 25% fine sand for the U2 position. These traces show how the magnitudes of the steady-state measured pore pres-
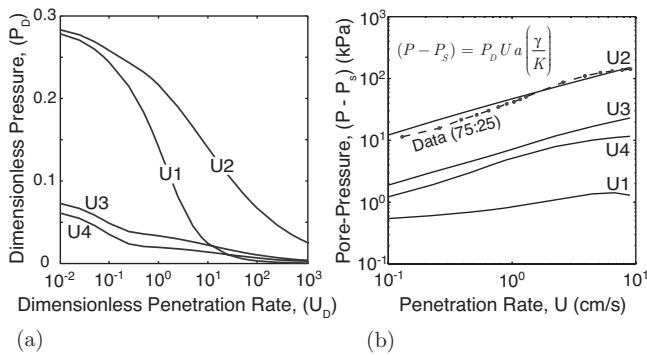
**Fig. 5.** FEM traces of penetration induced pore pressure as a function of penetration rate for cone tip (U1), shoulder (U2), and shaft (U3 and U4) positions shown in (a) dimensionless $P_D - U_D$ space; (b) dimensional $(p - p_s)$-U space; compared with centrifuge laboratory data obtained from mini-CPTu tests conducted in a sample of 75% kaolin mixed with 25% fine-sand (dot-dashed line)



**Fig. 6.** FEM calculated contour plots of the steady-state fluid-pressure field induced around the penetrating cone tip illustrating the transition from dissipation governed pressure response $(U_D \cdot 10^{-1})$ to an advection governed pressure response $(U_D \cdot 10^{-1})$. $P_D$ values listed in each pane represent the maximum and minimum contours values.

sures are governed by either diffusivity when penetration rate is constant (such as for a typical CPTu test), or via penetration rate when diffusivity magnitudes are constant (such as in a homogeneous soil).

The steady-state pressure magnitudes match the terminal pressure magnitudes recovered from the buildup response. Fig. 5(a) shows the relationship that exists between penetration rate and the stable pressure magnitudes at locations along the cone tip and shaft at the U1, U2, U3, and U4 locations (see Fig. 2). The induced pore-pressure response at the cone surface and surrounding region is controlled by the rate of penetration, as detailed in the previous section. Fig. 5(a) shows the inverse proportionality between dimensionless penetration rate and steady dimensionless induced pressures along the cone surface. Fig. 5(b) shows the proportional relationship that exists once the dimensionless pressure has been converted to a dimensional pressure. In the dimensional case, there is a direct relationship showing that increasing $U_D$ causes an increase in the steady-state dimensional induced pore-pressure observed at the cone tip and shoulder positions. The stable pressure fields that develop are a combined effect of the rate at which fluid is injected through the tip of the probe, representing the large strain deformation of the medium, and the rate at which the soil advects past the tip-local process zone, representing the advance of the cone in the medium.

At dimensionless penetration rates below the threshold of $U_D \cong 10^{-1}$, the steady response is pressure diffusion dominated and the geometry of the pressure bulb is uniformly symmetric. The pressure distributions are identical and are similar to the spherically symmetric response apparent in other steady solutions (Elsworth and Lee 2005) where fluid is assumed injected into the process zone at a rate governed by the penetrometer advance. These data have been used in the reduction of CPTu metrics to yield profiles of in situ permeability. Importantly, these prior models have assumed simplified spherical geometry and result in a single pore-pressure profile when viewed in terms of dimensionless pressures (top two of panes in Fig. 6). The spatial distributions of pressure are shown over the same range of dimensionless penetration rates in Fig. 6.

Clearly this is a simplification. Two factors affect this response. The first is that the analysis is unable to accommodate the true geometry of the tip-local process zone and there is a small effect related to this. More important is the role of advection in advecting low fluid content material into the process zone and in
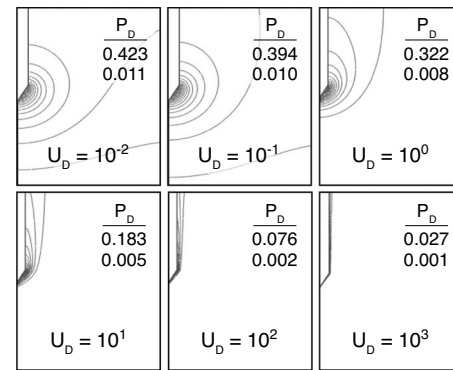
advecting elevated fluid content material out form the zone. This results in the evolution of the nonspherical symmetry apparent at higher penetration rates, when the fluid pressure zone becomes elongated.

Another important finding is the observed variation in pore-pressure magnitude as a function of location along the cone surface in combination with penetration rate. This relationship is shown in a comparison of the profiles for the U1, U2, U3, and U4 positions in Figs. 5(a and b). Peak pressure magnitudes reduce relative to the peak threshold magnitude of penetration rate, $U_D$, and drop more precipitously for the tip location, U1, relative to the shoulder mounted location, U2. This is primarily related to the role of the advection of porous medium undercharged with porous mass, the U1 location is reached by this earliest. The dependence of location on the pore-pressure magnitudes along the cone surface has previously been documented (Levadoux and Baligh 1986) for undrained analysis, although the influence of concurrent drainage has not been analyzed. This analysis identifies the important influence of the advection soil on the resulting fluid pressure response.

### Dissipation Response

Dissipation of the induced pore-pressure field is an important component in understanding the mechanisms by which pore pressures equilibrate around the tip. These data are typically used to recover magnitudes of consolidation coefficient, or hydraulic diffusivity, from field data. The postarrest dissipation response induced by the penetrating cone was investigated by allowing the model to reach steady-state pressure magnitudes; then the advection of the medium and the injection of the fluid through the cone tip were simultaneously halted. The dissipation of the pore-pressure field was recorded until background pressures were reached at the cone tip. Traces of dimensionless pressure dissipation are shown for the full range of prepenetration rates, $10^{-2} \leqslant U_D \leqslant 10^3$ in Fig. 7 [(a.1)–(c.1)] for three monitoring locations, with respect to the product of the dimensionless time after postarrest $(t'_D)$ and the dimensionless penetration rate $(t'_D U_D)$. The dimensionless pressure traces are also recast in dimensional form and shown in Fig. 7 [(a.2)–(c.2)].

Review of the dimensional traces of pore-pressure dissipation with respect to time following postarrest illustrate a few important aspects of fluid transport properties of soils. First, it is seen here
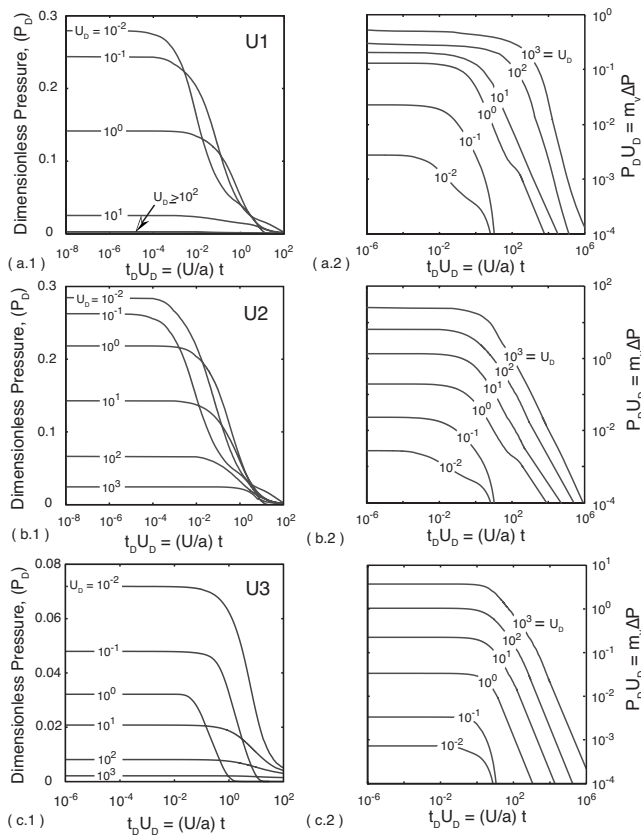
**Fig. 7.** Traces of pore-pressure dissipation trends following penetration arrest for the (a) cone tip (U1); (b) cone shoulder (U2); and (c) five penetrometer radii behind shoulder ($X_D=5$) (U3) positions. The pore-pressure dissipation trends are shown for [(a.1)–(c.1)] dimensionless pressure and [(a.2)–(c.2)] for a scaled dimensional pressure with respect to a scaled time factor ($t_D U_D$).



**Fig. 8.** Dissipation response of pore-pressure field following penetrometer arrest. Magnitudes of pore-fluid pressures are for the upper and lower contoured intervals of dimensionless pressure.

that soil drainage is highly influential in governing the peak magnitude of pore pressure prior to penetration arrest, when penetration rate is constant. These peak magnitudes of pore pressure then being to dissipate with time following penetration arrest in a near linear trend when viewed in $\log(P_D)-\log(t'_D U_D)$ space, and systematically offset for each increase in $U_D$. The second important point here is that the time for dissipation to background levels varies as a function of $U_D$ which is logical as higher pore pressures require longer times to dissipate. The important factor in this is that for recovering consolidation coefficients from CPTu tests via methods correlating $t_{50}$ to $C_v$ (such as Teh and Houlsby 1991) the value of $t_{50}$ obtained will be highly dependant on reaching undrained conditions prior to halting penetration.

The dependence of the spatial distribution on the pore-pressure dissipation is a function of the penetration rate, the time after postarrest ($t'_D$), and the location in reference to the tip-local process zone. Dissipation of the pore-pressure field is shown to be dependent on the penetration rate that generated the primary pore-pressure field. This corollary may be surmised from the contour results of Fig. 8, in which the dissipation field transits from a purely spherical to a mainly radial field with increases in penetration rate; and predicted by the pressure response curves in Fig. 7 [(a.1)–(c.1)] where the rate of dissipation is accelerated as the prearrest penetration rate increases. Importantly, this contradicts the contention that a single (unique) response curve, fixed in dimensionless time, may adequately represent the dissipation of
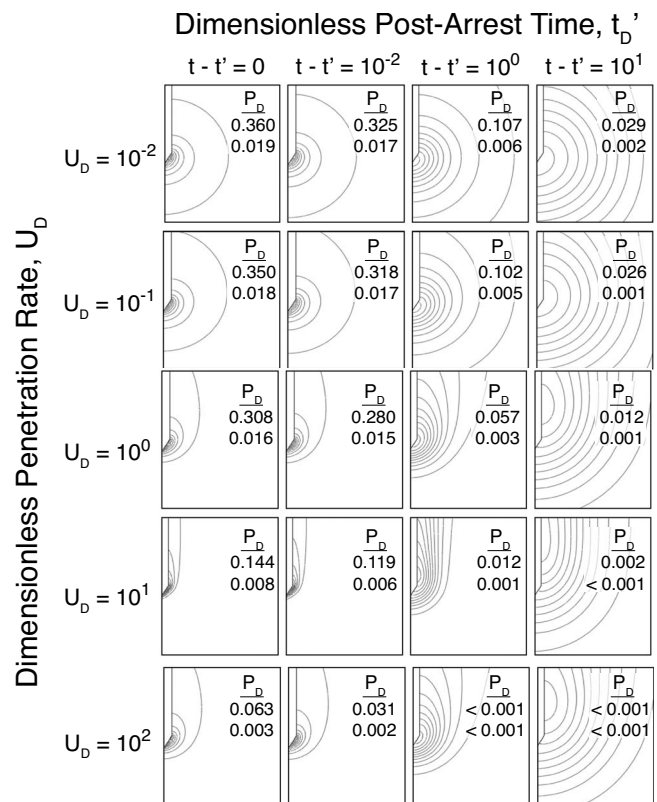
pore pressures on the cone shaft. Similar to the generation of pore pressures, a threshold dissipation behavior is apparent for prearrest penetration rates $U_D \le 10^{-1}$, and is a result of identical initial pressure distributions preceding the dissipation process, resulting in a single pressure-dissipation response fixed in dimensionless time. This behavior is apparent in Fig. 7 [(a.2)–(c.2)].

### Correlation of Pore Pressure with (Coefficient of) Permeability

The observation that peak shaft pore-pressure magnitudes are dependent only on (coefficient of) permeability, penetration rate, and penetrometer geometry suggest that (coefficient of) permeability magnitudes may be recovered from shaft data. Elsworth and Lee (2005) derived a relationship to recover dimensionless magnitudes of (coefficient of) permeability ($K_D$) from the product of the normalized pore pressure, $B_q=(p-p_s)/(q_t-\sigma_{vo})$, and the normalized end-bearing indices, $Q_t=(q_t-\sigma_{vo})/\sigma'_{vo}$, where $B_q Q_t =(p-p_s)/\sigma'_{vo}=\alpha/(1+K_D)^\beta$ with coefficients $(\alpha,\beta)$ initially assumed as unity. The dimensionless index $K_D$ is directly proportional to the (coefficient of) permeability ($K$) through the relationship $K_D=(4K\sigma'_{vo})/(Ua\gamma_w)$ (Elsworth and Lee 2005), where $\sigma'_{vo}=$ vertical effective stress, $U=$ penetration rate, $a=$ radius of the penetrometer, and $\gamma_w=$ unit weight of water. Figs. 9(a–c) show the relationship between $B_q Q_t$ and $K_D$ for steady-state peak pressure magnitudes determined, from the model results contained within this paper, for the three cone penetrometer locations U1, U2, and U3. Here the $B_q Q_t-K_D$ relationship is shown for the range of dimensionless penetration rates from $10^{-2} \le U_D \le 10^3$. The solution has been demonstrated to be valid only for partially drained conditions where $B_q Q_t < 1$. For
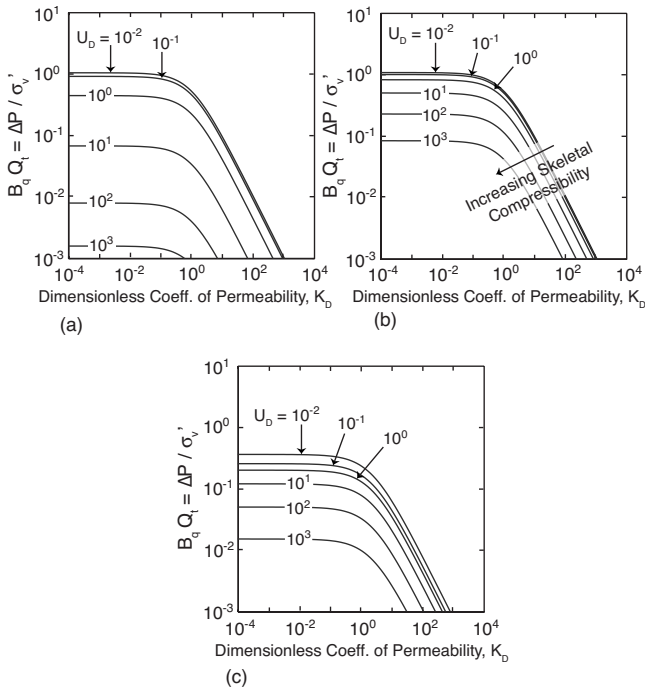
Fig. 9. Profiles representing the relationship between the cone metrics $B_qQ_t$ and dimensionless permeability $K_D$ for port locations (a) U1; (b) U2; and (c) U3. Dimensionless penetration rates in the range of $10^{-2} \leqslant U_D \leqslant 10^3$ showing the theoretical influence of skeletal compressibility on resulting profiles.
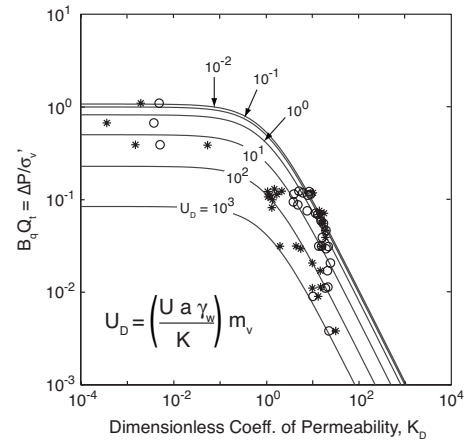


Fig. 10. Profiles of $U_D$ obtained from the modeling results contained in this paper expressed in $B_qQ_t-K_D$ space. These traces illustrate the influence of system compressibility on the ability to recover coefficient of permeability magnitudes directly from CPTu metrics during continuous advance. These profile traces are compared against CPTu data collected at the GEMS testing site in Lawrence, Kan. from July 2005 (Lee et al. 2007) with independently obtained measurements of $K$ for each data point.

magnitudes of $B_qQ_t \geqslant 1$ the response is undrained, and controlled primarily by failure around the advancing tip (Lee et al. 2007), and solutions similar to that presented here cease to be valid.

A review of Figs. 9(a–c) shows that the relationship for the three cone locations (U1, U2, and U3), at very low penetration rates, $U_D \leqslant 10^{-1}$ begin to collapse to a single line. Additional model results for $U_D \leqslant 10^{-2}$ (not shown here) support this observation and reduce to a single curve at $U_D = 10^{-2}$. Within these profiles the $U_D$ traces may be recast to express the influence that skeletal compressibility has on the position of the resulting traces by combining $K = C_v m_v \gamma_w$ with Eq. (11) to yield

$$U_D = \left( \frac{U a \gamma_w}{K} \right) m_v \qquad (22)$$

Here it can be seen that for conditions of constant penetration rate $(U)$ and permeability $(K)$ that the compressibility may be isolated as the underlying parameter which affects the peak magnitudes of $B_qQ_t$ at the undrained limit. This can be further supported through comparison with an analytical model presented based on cavity expansion methods (Elsworth and Lee 2007) as

$$B_qQ_t = \left( \frac{4}{3} \right) \frac{S_u}{\sigma_v'} \ln \left( \frac{G}{S_u} \right) \qquad (23)$$

and at the undrained limit $G = E/3 = 1/(3m_v)$ allowing the undrained peak magnitude of $B_qQ_t$ for each order of magnitude increase in $U_D$ to be expressed as

$$B_qQ_t = \left( \frac{4}{3} \right) \frac{S_u}{\sigma_v'} \ln \left( \frac{U a \gamma_w}{3K S_u U_D} \right) \qquad (24)$$

A simple review of Eq. (24) indicates that as $U_D$ is increased the

resulting undrained peak magnitude of $B_qQ_t$ will be reduced which supports the independently modeled results in Figs. 9(a–c).

This represents the case for the influence of penetration rate, in the low $U_D$ region, where fluid mass storage effects of the medium have little influence on the solution for recovering $K_D$ values from the CPTu-recovered data. Absent storage effects, the induced pore-fluid pressure response is directly proportional to penetration rate, and inversely proportional to (coefficient of) permeability. In the case of the low $U_D$'s, the pore-pressure field has completely developed and the pressure gradient is the same for $U_D$'s below this threshold limit. Penetration rates above this limit are influenced primarily by the rate of fluid mass deficient material into the process zone. As a result the pressure differential between the near and far field is reduced requiring this effect to be accommodated into the reduction of data at high system compressibilities, or possibly also low diffusivities.

### Validation

The model is validated against CPTu data recovered from the GEMS site [a joint Kansas Geological Survey's (KGS) and Kansas State University's (KSU) field site] located in Lawrence, Kansas. The CPTu data include the end-bearing magnitudes $(q_t)$, and the pore-pressure magnitudes $(p - p_s)$ for the shoulder position on the cone (U2 position), from soundings conducted in July 2005. The data were collected using industry standard procedures for CPTu operation, under an almost constant penetration rate of 2 cm/s. The end-bearing and pore-pressure data were averaged over 4-cm intervals to limit the "noise" in the sounding (Lee et al. 2007). Fig. 10 shows the relationship between $B_qQ_t$ and $K_D$ resulting from the peak pressure magnitudes observed at the U2 position. Permeabilities were measured independently via constant head flow-through tests conducted using a direct push slug test system with the ability to provide localized (4- and 1-cm-tall screens) measurements (Lee et al. 2007).

A comparison of the field data with the $B_qQ_t-K_D$ relationship shows a general clustering of data near the asymptotic line

$U_D = 10^{-2}$ where the pore-pressure field is predicted as fully developed, with respect to the penetration rate. The deviation of the remaining data away from this line is considered to be the combined effect of tip geometry and of storage effects, detailed previously. These are not included in the development of the simple relationship $B_q Q_t = \alpha / (1 + K_D)^\beta$ (Elsworth and Lee 2005). However, in light of these two influences, the data do fit within the range predicted by the modeling results developed here, and constrained by the upper threshold limit of $U_D = 10^3$. These suggest the importance of accommodating storage effects around the tip in representing real field data.

## Conclusions

The development of a model which can accurately predict the influence of cone tip geometry and penetration rate on the magnitudes of induced pore-pressure fields surrounding an advancing cone is of critical importance in reducing CPTu-recovered data. The analysis presented here develops a sound framework to use in the prediction of pore-pressure fields induced during cone penetration in a saturated linearly elastic medium. Some shortcomings of this analysis are the inability to generate fluid pressures within the porous medium and around the process zone, as a direct result of compaction. The approximate solution, accommodating continuity through the injection of tip-local fluid pressures, is shown to correlate with field observations.

The principal observations of this study are the following. First, dimensionless penetration rate strongly influences the magnitude of induced pore-fluid pressure above a threshold limit of $U_D > 10^{-1}$. Penetration rates below this limit converge to a single steady dimensionless pressure magnitude. This is of the order $P_D \sim 1/4$ and is broadly congruent with simple spherical solutions absent storage or tip geometry effects. At higher penetration rates, the role of fluid storage in the advecting medium exerts an important influence, reducing the magnitude of dimensionless pressure. Second, for all $U_D$'s, the magnitude of the pore-pressure field surrounding the cone varies as a function of location along the cone surface, which has been experimentally observed. Third, for using predictions of $B_q Q_t$ to determine $K$, storage effects are shown to be significant. At $U_D > 10^{-1}$ the predictive relation is offset from the simplified relation $B_q Q_t = \alpha / (1 + K_D)^\beta$. This is apparent in the influence of $U_D$ on this relationship, illustrated in Figs. 9(a–c). Also at high $U_D$'s the time to reach steady state is extended and pore pressures may be recorded which are prepeak (lower than peak pressure). Thus $K_D$ magnitudes predicted from the assumption that pressures have actually reached steady state will be in error; permeabilities will be predicted to be higher than actual. Fourth, dissipation of the pore-pressure field surrounding the cone in postarrest conditions is strongly influenced by $U_D$. Together, these effects have important implications on the recovery of $K$ profiles from cones sounding metrics.

The results of this study are congruent with observations of CPTu tests and are important in illustrating the effect of both skeletal compressibility and diffusivity on the pressure fields induced from the advancing probe. These provide important input in interpreting peak magnitudes of pore pressure recorded at various locations along the cone surface. Importantly, these analyses guide the use of measured pore pressures in predicting $K$ profiles form cone sounding data, suggesting that in certain circumstances, skeletal compressibility ($m_v$), penetration rate ($U$), and consolidation coefficient ($C_v$) influence the reduction of CPTu data.

## Notation

*The following symbols are used in this paper:*

$a$ = radius of the penetrometer $[L]$;
$B_q$ = dimensionless pore-pressure ratio $(p - p_s)/(q_t - \sigma_{v0})$;
$C_V$ = coefficient of consolidation $[L^2 T^{-1}]$;
$c$ = hydraulic diffusivity, $c = k_i/(\mu m_v) = (k_i/\mu)K$ $[L^2 T^{-1}]$;
$K$ = (coefficient of) permeability $[L T^{-1}]$;
$K^{\text{bulk}}$ = drained bulk modulus $[M L^{-1} T^{-2}]$;
$K_D$ = dimensionless (coefficient of) permeability $K_D = (4 K \sigma'_{vo})/(U a \gamma_w)$;
$k_i$ = intrinsic permeability $[L^2]$;
$l$ = length $[L]$;
$l_D$ = dimensionless length, $l_D = l/a$;
$m_v$ = coefficient of volume compressibility $[M^{-1} L T^2]$;
$P_D$ = dimensionless pressure, $P_D = (k_i/\mu)[(p - p_s)/U a]$;
$p$ = absolute pore-fluid pressure $[M L^{-1} T^{-2}]$;
$p_s$ = initial static fluid pressure $[M L^{-1} T^{-2}]$;
$Q_D$ = dimensionless flux;
$Q_t$ = dimensionless penetrometer end-bearing resistance $(q_t - \sigma_{v0})/\sigma'_{v0}$;
$q_i$ = convective flux $[L T^{-1}]$;
$q_t$ = penetrometer end-bearing stress $[M L^{-1} T^{-2}]$;
$R_D$ = dimensionless radial component, $R_D = r/a$;
$r$ = radial component between origin and point, $r^2 = \Sigma x_i^2$;
$t$ = time $[T]$;
$t_D$ = dimensionless time, $t_D = C_v t/a^2$;
$t'_D$ = time after post arrest;
$U$ = cone penetration rate $[L T^{-1}]$;
$U_D$ = dimensionless penetration rate, $U_D = U a/C_v$;
$v_i$ = fluid-solid mixture velocity vector $[L T^{-1}]$;
$v_i^f$ = fluid velocity vector $[L T^{-1}]$;
$x_D$ = dimensionless coordinate system, $x_D = x_i/a$;
$x_i$ = coordinate system;
$\beta_f$ = coefficient of fluid compressibility $[M^{-1} L T^2]$;
$\gamma_w$ = unit weight of water $[M L^{-2} T^{-2}]$;
$\mu$ = dynamic viscosity $[M L^{-1} T^{-1}]$;
$\rho$ = density of soil-water mixture $[M L^3]$;
$\sigma_{v0}, \sigma'_{v0}$ = initial vertical stress and effective stress $[M L^{-1} T^{-2}]$; and
$\phi$ = porosity.

## References

Acar, Y. B., and Tumay, M. T. (1986). "Strain field around cones in steady penetration." *J. Geotech. Engrg.*, 112(2), 207–213.

Baligh, M. M. (1985). "Strain path method." *J. Geotech. Engrg. Div.*, 111(9), 1108–1136.

Baligh, M. M., and Levadoux, J. N. (1986). "Consolidation after undrained piezocone penetration. II: Interpretation." *J. Geotech. Engrg.*, 112(7), 727–745.

Baligh, M. M., and Scott, R. F. (1976). "Analysis of deep wedge penetration in clay." *Geotechnique*, 26(1), 185–208.

Biot, M. A., and Willis, D. G. (1957). "The elastic coefficients of the theory of consolidation." *J. Appl. Mech.*, 24, 594–601.

Chen, B. S.-Y., and Mayne, P. W. (1994). "Profiling the overconsolidation ratio of clays by piezocone test." *Rep. No. GIT-CEE/GEO-94-1*, Georgia Institute of Technology, Atlanta.

Drescher, A., and Kang, M. (1987). "Kinematic approach to limit load for steady penetration in rigid-plastic soils." *Geotechnique*, 37(3), 233–246.

Elsworth, D. (1991). "Dislocation analysis of penetration in saturated porous media." *J. Eng. Mech.*, 117(2), 391–408.

Elsworth, D. (1992). "Pore pressure response due to penetration through layered media." *Int. J. Numer. Analyt. Meth. Geomech.*, 16, 45–64.

Elsworth, D. (1998). "Indentation of a sharp penetrometer in a poroelastic medium." *Int. J. Solids Struct.*, 35(34–35), 4895–4904.

Elsworth, D., and Lee, D. S. (2005). "Permeability determination from on-the-fly piezocone sounding." *J. Geotech. Geoenviron. Eng.*, 131(5), 643–653.

Elsworth, D., and Lee, D. S. (2007). "Limits in determining permeability from on-the-fly CPTu sounding." *Geotechnique*, 57(8), 679–685.

Ladanyi, B. (1963). "Expansion of a cavity in a saturated clay medium." *J. Soil Mech. and Found. Div.*, 89(4), 127–161.

Lee, D. S., Elsworth, D., Hryciw, R. D., and Butler, J. (2007). "Hydraulic conductivity measurements from on-the-fly CPTu and from VisCPT." *J. Geotech. Geoenviron. Eng.*, 134(12), 1720–1729.

Levadoux, J. N., and Baligh, M. M. (1986). "Consolidation after undrained piezocone penetration. I: Prediction." *J. Geotech. Engrg.*, 112(7), 707–725.

Lunne, T., Robertson, P. K., and Powell, J. J. M. (1997). *Cone penetration testing in geotechnical practice*, Taylor & Francis, London.

Randolph, M., and Hope, S. (2004). "Effect of cone velocity on cone resistance and excess pore pressures, IS-Osaka 2004." *Proc., Int. Symp. on Engineering Practice and Performance of Soft Deposits*, Osaka, Japan, 147–152.

Randolph, M. F., and Wroth, C. P. (1979). "Analytical solution for the consolidation around a driven pile." *Int. J. Numer. Anal. Methods Geomech.*, 3(3), 217–229.

Robertson, P. K., Campanella, R. G., Gillespie, D., and Greig, J. (1986). "Use of piezometer cone data." *Proc., Use of In Situ Tests in Geotechnical Engineering*, ASCE, New York.

Robertson, P. K., Sully, J. P., Woeller, D. J., Lunne, T., Powell, J. J. M., and Gillespie, D. G. (1992). "Estimating coefficient of consolidation from piezocone tests." *Can. Geotech. J.*, 29(4), 539–550.

Skempton, A. W. (1954). "The pore pressure coefficients A and B." *Geotechnique*, 4, 143–147.

Teh, C. I., and Houlsby, G. T. (1991). "An analytical study of the cone penetration test in clay." *Geotechinque*, 41(1), 17–34.

Torstensson, B. A. (1977). "The pore pressure probe." *Proc., Geoteknikkdagan 1977*, Norwegian Society of Soil and Rock Technology, Oslo, 34.1–34.15.

Tumay, M. T., Acar, Y. B., Cekirge, M. H., and Ramesh, N. (1985). "Flow field around cone in steady penetration." *J. Geotech. Engrg. Div.*, 111(2), 193–204.

Vesic, A. S. (1972). "Expansion of cavities in infinite soil mass." *J. Soil Mech. and Found. Div.*, 98, 265–290.